Electroreflectance study of silicon nanocrystals

2007 J. Phys.: Condens. Matter 19 445005

(http://iopscience.iop.org/0953-8984/19/44/445005)

IOP PUBLISHING JOURNAL OF PHYSICS: CONDENSED MATTER

J. Phys.: Condens. Matter **19** (2007) 445005 (16pp) doi:10.1088/0953-8984/19/44/445005

Electroreflectance study of silicon nanocrystals

T Toyama and H Okamoto

Department of Systems Innovation, Graduate School of Engineering Science, Osaka University, Toyonaka, Osaka 560-8531, Japan

E-mail: toyama@ee.es.osaka-u.ac.jp

Received 31 October 2006, in final form 20 February 2007
Published 18 October 2007
Online at stacks.iop.org/JPhysCM/19/445005

Abstract

Electroreflectance (ER) measurements were performed on Si nanocrystals with a crystal size of about 1–3 nm to reveal their electronic structure. Interband transitions arising from confined electron–hole (e–h) pairs were observed clearly at room temperature as the discrete features located between 1.2 and 3.1 eV. Theoretical analyses elucidated the reduced mass, kinetic energies and Coulomb attraction energies of the confined e–h pairs. Extra ER features were also observed from Si nanocrystals at 3.4 eV, indicating that $E_1(E_0')$ direct gaps remain in the Si nanocrystals. Moreover, effects on ER signals of impurity doping and oxidation, which usually influence optical properties, are described. The ER technique is also applied to plasma-deposited Si thin films. Finally, an extended experimental technique, grazing-angle-incident polarized ER spectroscopy, is demonstrated.

(Some figures in this article are in colour only in the electronic version)

1. Introduction

Since the first discovery of strong luminescence at room temperature with emission energies larger than the bandgap of crystalline Si (c-Si) [1, 2], the optical properties of Si nanocrystals such as those formed in porous Si have been studied intensively as physical phenomena arising from quantum confinement (QC) effects in low-dimensional indirect semiconductors [3–5]. Specifically, two interesting phenomena are apparent for Si nanocrystals with reduced crystal sizes: an increase in the kinetic energy of confined electron–hole (e–h) pairs caused by QC effects and, at the indirect bandgap, the appearance of a quasi-direct transition, which is attributable to partial breakdown of the $\boldsymbol{k}$-conservation rule as a result of spatial confinement in real space. Spectroscopic studies are effective at revealing such a confinement-related nature.

In indirect semiconductors, spectroscopic measurements are strongly influenced by the optical transitions at higher critical points [6]. In bulk c-Si, the maximum point of the valence band is located at the Γ-point, the centre of the Brillouin zone, whereas the minimum points of the conduction band are located near the X-point, at (0.86, 0, 0) π/a points. With respect

to the interband transitions at the fundamental gap of $E_{g(G-X)}$, the spectral features appear as weakly associated with the indirect nature in comparison to the spectral features attributed to the direct transitions at the zone centre (E_0' and E_0 gaps), along the $\langle 111 \rangle$ direction (E_1 gap), and along the $\langle 100 \rangle$ direction (E_2 gap). Regarding Si nanocrystals, spectral features arising from the fundamental gap have not been observed clearly, but spectral features attributed to the $E_1(E_0')$ and E_2 direct gaps have been identified in optical reflectance [7] and ellipsometry spectra [8]. Almost no experiments have been carried out to extract optical transitions at the fundamental gap in Si nanocrystals individually from the optical transitions at higher critical points.

It is therefore necessary to introduce an experimental approach with high spectral resolution for extraction of the QC-related structure from the unresolved optical spectral line shape. Electroreflectance (ER) spectroscopy is particularly useful for high-resolution optical spectroscopy because the obtained line shapes reflect the derivative of the unperturbed dielectric function [6, 9, 10]. The structure-less background is thereby largely reduced and sharp peaks appear at the interband critical points. In addition, spectral structures of confined systems (e.g. excitons, sub-band states in quantum wells) can be extracted using ER spectroscopy [10].

This paper presents a review of ER studies of Si nanocrystals [11–20]. The Si nanocrystals, with a small size distribution, were prepared by anodization. The mean crystal sizes of about 1–2 nm were confirmed using a transmission electron microscope (TEM) [15, 17]. We examined ER features taken from Si nanocrystals found in the infrared to visible (IR–vis) region in conjunction with the mean crystal sizes of the Si nanocrystals. The origins of confined e–h pairs in Si nanocrystals are discussed along with extra ER features in the ultraviolet (UV) region, for which transition energies are almost independent of the crystal size, which are related to the three-dimensional electronic structure of the Si nanocrystals. Furthermore, the effects of impurity doping [16, 20] and oxidation [18], which usually influence photoluminescence (PL) properties [3–5], on ER features are explained herein. Results for plasma-deposited Si thin films and subsequent anodization are also described [11–14]. Finally, an additional experimental technique, grazing-angle-incident polarized ER spectroscopy, is explained [19]. This technique particularly enhances optical transitions in Si nanocrystals located at surface regions of the anodized layer.

2. Experimental details

2.1. Experimental setup

Figure 1(a) depicts the experimental configuration used for ER measurements [6, 10]. Monochromatic light from a tungsten–halogen lamp or xenon lamp irradiated the sample; the reflected light was then detected by a Si or InGaAs photodiode. A DC bias voltage, V_{DC}, of -10 V and a modulation ac voltage, ΔV_{pp}, of 5 V were applied. The modulation frequency was 500 Hz. The ER signal, $\Delta R/R$, was obtained from the reflectance component, R, and the modulation component, ΔR. ER measurements were mainly taken at 293 K, or between 4 and 293 K, after cooling using a closed-cycle helium refrigerator (Cryotec; Daikin Industries Ltd).

The sample structure for the ER measurement is displayed schematically in figure 1(b). Anodized layers containing Si nanocrystals were prepared from p-type boron-doped (100) substrates with resistivities of 4–10 Ω cm. Aluminium was evaporated onto the rear surface of the substrate, then sintered at 500 °C for 5 min in a vacuum. The resulting Al acts as an ohmic back contact during anodization as well as during ER measurements. Anodization was performed in a conventional electrolytic cell [3–5]. The crystal sizes were controlled to 1–3 nm

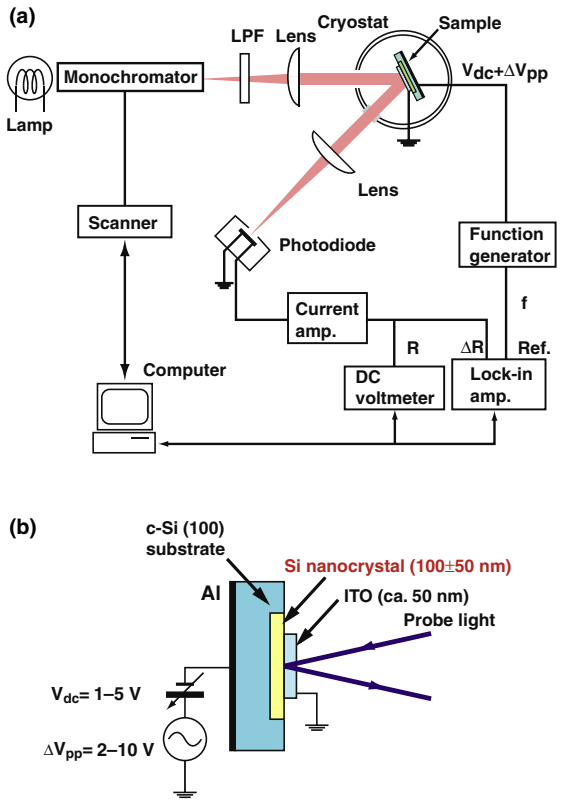

Figure 1. Schematic illustrations of the experimental setup for ER measurement (a) and sample structure (b).

Table 1. Anodizing conditions and crystal sizes of two samples used in figures 2–4. Here J_{anod} denotes the anodizing current density, t_{anodiz} the anodizing time, L_m is the mean crystal size estimated from the TEM image and L_0 is the crystal size estimated from the ER measurement.

Sample	J_{anod} (mA cm^{-2})	t_{anod} (s)	L_m (nm)	L_0 (nm)
A	3.25	15	1.3	1.7
B	81.2	1.0	2.3	2.3

using the anodizing current density, J_{anod}. The anodizing current densities were varied in the range of 3.25–81.2 mA cm^{-2}. Hydrofluoric acid (HF) in an electrolytic aqueous or ethanol solution was used at typical concentration of 12.5%. More highly concentrated HF solutions up to 37.5% were used for changing the crystal size slightly. Finally, indium tin oxide (ITO) was evaporated onto the anodized layer in an oxygen atmosphere at 200 °C as a transparent conductive oxide (TCO) cathode. The typical ITO thickness was about 50 nm.

The anodized layers were as thin as 100 ± 50 nm, as measured from cross-sectional views taken using a field-emission scanning electron microscope (FESEM; JEM6340F, JEOL) or a TEM (H-9000NAR, Hitachi Ltd) because the size distribution of nanocrystals is suppressed in such thin anodized layers. To maintain the thickness, the anodizing time t_{anod} was varied between 15 and 1.0 s; t_{anod} was decreased for increased J_{anod}. In table 1, t_{anod} and J_{anod} values are shown for two typical samples. Using the thin anodized layer yields some other advantages

for optical measurements: (1) a weak contribution of optical interference; (2) a reduction in optical scattering loss resulting from surface roughness; and (3) from the IR to blue region, the entire anodized layer in the growth direction can be monitored because the penetration depth of the probe light is greater than the layer thickness. Also, in association with ER measurements: (4) modulation electric fields are applicable to the thin anodized layer using low applied voltages.

Raman scattering measurements were taken using Renishaw microscope systems; the 325 nm line of the He–Cd laser and the 514.5 nm line of the Ar^+-ion laser were used as the excitation sources.

2.2. Line shape analysis

The ER spectra were analysed using the following conventional line shape analysis [6, 9, 10]. The relationship between the ER signal, $\Delta R/R$, and the corresponding modulation of dielectric function ($\varepsilon(=\varepsilon_1 + i\varepsilon_2)$) is expressed as [6, 9, 10]

$$\frac{\Delta R}{R} = \alpha\Delta\varepsilon_1 + \beta\Delta\varepsilon_2, \tag{1}$$

where $\Delta\varepsilon_1$ and $\Delta\varepsilon_2$, respectively, denote the modulation components of the real and imaginary parts of the dielectric function, and α and β are the Seraphin coefficients. If the dielectric function is approximated as a Lorentzian line shape, the ER signal obtained for low electric fields can be expressed as [9]

$$\frac{\Delta R}{R} = \mathrm{Re}[Ce^{i\theta}(E - E_g + i\Gamma)^{-m}], \tag{2}$$

where E denotes the photon energy of the probe light, E_g is the transition energy, Γ represents the broadening parameter and C and θ, respectively, denote the amplitude and phase parameters, depending only weakly on E. The exponent $m = 2.5$ is used for the E_0' transition, $m = 3$ for the E_1 transition [21] and $m = 2$ for the confined system [6, 10]. The observed ER spectrum was decomposed numerically into a combination of some spectral components using a nonlinear least-squares fitting method.

3. Electroreflectance of Si nanocrystals

3.1. Size distribution

Figure 2 shows cross-sectional TEM images of two samples fabricated with the anodization conditions listed in table 1 [15]. No void was found in the anodized layers of either sample. With an increase in J_{anod} (and a decrease in t_{anod}), the crystalline part in the anodized layer is increased. The magnified images of the left figures in figure 2 show lattice fringes corresponding to the (111) planes of Si nanocrystals embedded in amorphous tissue of silicon oxide (and/or hydride). The crystal size, L, is defined as the diameter of a circle with an area that is equal to that of a nanocrystal. Figure 3 shows the size distribution of Si nanocrystals, as estimated from the TEM images. The size distribution is well expressed by the following log-normal function, which is generally used for the size distribution of fine particles [22]:

$$f \sim \frac{1}{\sigma_m\sqrt{2\pi}} \exp[-(\ln L - \ln L_m)^2/2\sigma_m^2]. \tag{3}$$

Here f denotes the frequency. The mean crystal size, L_m, and the deviation, σ_m, are estimated, respectively, as $L_m = 1.3$ nm and $\sigma_m = 0.22$ for sample A and $L_m = 2.3$ nm and $\sigma_m = 0.67$ for sample B. Therefore, the mean crystal size tends to be smaller with lower anodizing current density (and with longer anodizing time).

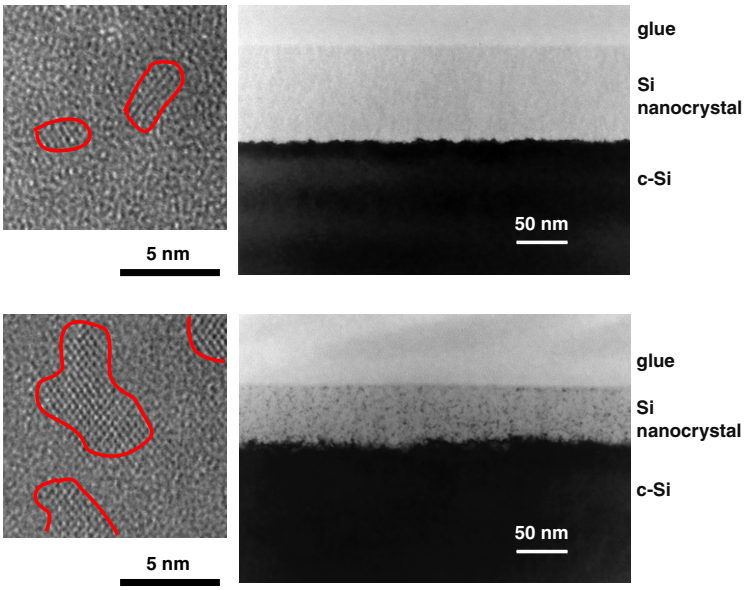

Figure 2. Cross-sectional TEM images of samples fabricated with different anodizing conditions, as listed in table 1 (sample A (top), sample B (bottom)). Left figures show lattice fringes corresponding to the (111) planes of Si nanocrystals. Solid lines drawn on the crystal boundaries are provided as a guide for the eye.

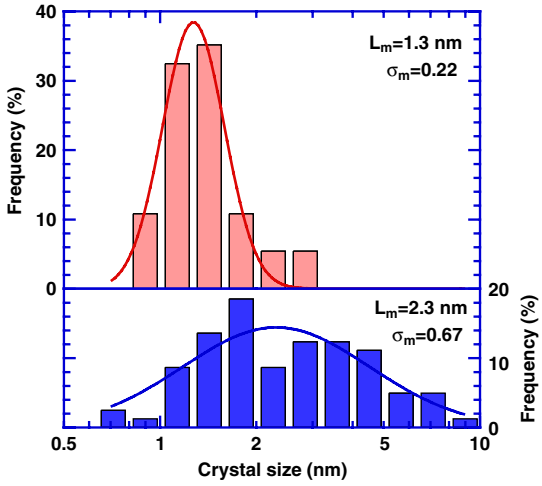

Figure 3. Size distribution of Si nanocrystals in samples A (top) and B (bottom) in table 1.

3.2. ER spectra

Figure 4 shows the ER spectra of Si nanocrystals produced under different anodizing conditions. Figure 4 also shows the ER spectrum of bulk c-Si measured with the ITO/c-Si diode. The IR–vis region between 1.2 and 3.1 eV contained two (sample A) and three (sample B) ER features, respectively, labelled in the latter case as E_{10}, E_{11} and E_{12}. The ER features in the IR–vis region have never been observed from the ER spectrum of c-Si. With increasing

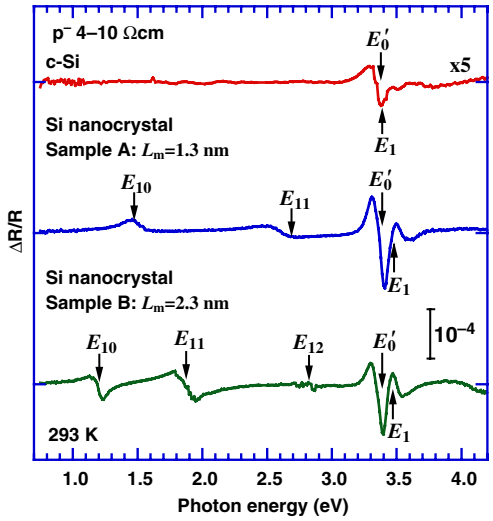

Figure 4. ER spectra of Si nanocrystals in samples A (middle) and B (bottom) in table 1. The top figure depicts the ER spectra of bulk c-Si. The ER spectra are intentionally offset for clarity. Arrows indicate transition energies estimated from line shape analyses ($E_{n\ell}$, transitions associated with confined e–h pairs; $E_1(E_0')$, transitions at the direct gaps).

mean crystal size, the transition energies of E_{10}, E_{11} and E_{12} features diminish; the energy distances, E_{11}–E_{10} and E_{12}–E_{11}, also diminish. Figure 4 also clearly displays a couple of ER features corresponding to optical transitions at $E_1(E_0')$ direct gaps at 3.4 eV [23]. Irrespective of the mean crystal size, the transition energies of $E_1(E_0')$ direct gaps are almost unchanged, although the broadening parameters are slightly larger than those observed for c-Si.

3.3. Optical transitions associated with confined e–h pairs

The size dependence of the ER features in the IR–vis region implies that E_{10}, E_{11} and E_{12} correspond to optical transitions associated with confined e–h pairs. We next tentatively assign E_{10}, E_{11} and E_{12} transitions to the transitions of the confined e–h pairs in a quantum dot. According to a simple effective mass approximation (EMA) model in the strong confinement region [24–26], the transition energy, $E_{n\ell}$, of the confined e–h pairs in the spherical quantum dot with an infinite-potential-height barrier is expressed as

$$E_{n\ell} = E_{g(\Gamma-X)} + \Delta E_{n\ell} - E_{\mathrm{Coul}} - E_{\mathrm{corr}}, \tag{4}$$

$$\Delta E_{n\ell} = \frac{2\hbar^2}{m^*}\left(\frac{\pi}{L_0}\xi_{n\ell}\right)^2 \qquad n = 1, 2, 3, \ldots, \quad \ell = 0, 1, 2 \ldots, \tag{5}$$

$$E_{\mathrm{Coul}} = C_{n\ell}e^2/\varepsilon L_0, \qquad \text{and} \tag{6}$$

$$E_{\mathrm{corr}} = 0.248E_{\mathrm{R}}, \tag{7}$$

where $E_{g(\Gamma-X)}$ denotes the fundamental gap of bulk c-Si (1.12 eV at 293 K), $\Delta E_{n\ell}$ is the kinetic energy of the confined e–h pairs, E_{Coul} is the Coulomb attraction energy, E_{corr} is the correlation energy, E_{R} is the Rydberg energy, $\hbar$ is Planck's constant, m^* is the reduced mass, L_0 is the crystal size, n is the principal quantum number, ℓ is the azimuthal quantum number and ε represents the dielectric constant of Si ($=11.9\varepsilon_0$). The parameter $\xi_{n\ell}$ is the nth solution of $j_\ell(\pi\xi) = 0$, j_ℓ is the ℓth spherical Bessel function and is given as $\xi_{10} = 1$, $\xi_{11} \approx 1.43$ and

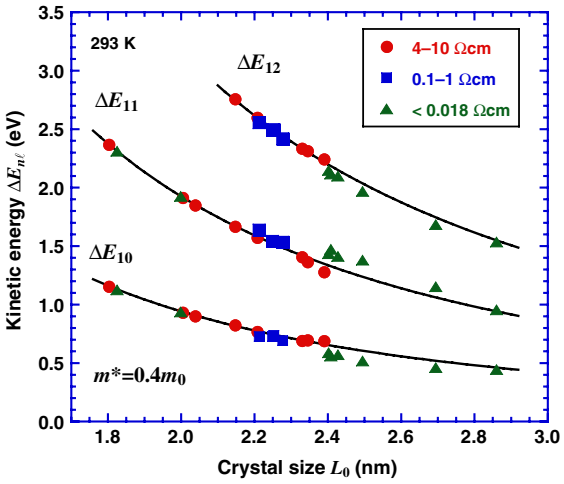

Figure 5. Kinetic energies, $\Delta E_{n\ell}$, of Si nanocrystals plotted against crystal size, L_0. The Si nanocrystals were fabricated from c-Si substrates with different resistivities (4–10 Ω cm, ●; 0.1–1 Ω cm, ■; <0.018 Ω cm, ▲). Solid lines are determined theoretically according to equation (5).

$\xi_{12} \approx 1.83$, respectively. The constant $C_{n\ell}$ in equation (5) is estimated as 3.57 for $n = 1$ and $\ell = 0$, and as 3.77 for $n = 1$ and $\ell = 1$ [26].

The crystal size, L_0, in equation (4) is deduced from the transition energies using the following procedure. Because $C_{n\ell}$ weakly depends on the quantum numbers for $n = 1$ and $\ell \leqslant 1$, we assume $C_{n\ell}$ as constant. Consequently, from equations (4) and (5), the transition energy, $E_{n\ell}$, can be expressed as a linear function against $\xi_{n\ell}^2$ with an intercept of $E_{g(\Gamma-\mathrm{X})} - E_{\mathrm{Coul}} - E_{\mathrm{corr}}$ and a linear coefficient of $2\pi^2\hbar^2/m^*L_0^2$. Applying $L_{\mathrm{m}} = 2.3$ nm, as inferred from the TEM image of sample B to L_0 in the linear coefficient, $m^* = 0.4m_0$ (m_0 is the electron mass) is obtained. Finally, putting $m^* = 0.4m_0$ into the linear coefficient of $2\pi^2\hbar^2/m^*L_0^2$, the value of L_0 for other samples is calculated. Furthermore, the effective Bohr radius, a_{B}^*, for the confined e–h pairs, which is expressed as

$$a_{\mathrm{B}}^* = \varepsilon\hbar^2/m^*e^2, \tag{8}$$

is given as 1.6 nm for $m^* = 0.4m_0$ at $L_0 = 2.3$ nm. Therefore, the fundamental assumption for the strong confinement region [24–26], $L_0 < 2a_{\mathrm{B}}^*$, is confirmed. In figure 5, the kinetic energies of the confined e–h pairs, $\Delta E_{n\ell}$, are plotted against L_0. It is noteworthy that the obtained m^* of $0.4m_0$ is available only at the calibrated size $L_{\mathrm{m}}(= L_0)$ of 2.3 nm, so that the relation of $\Delta E_{n\ell}$ against L_0 is not replaced by those against L_{m}, which is related to the so-called breakdown of the EMA model. On the other hand, we confirmed that the phenomenological relation, $\Delta E_{n\ell} \sim L_0^{-d}$ ($d < 2$), stands between $\Delta E_{n\ell}$ and L_0, which has often been found in the relation between the PL peak energy and the measured mean crystal size [3].

Figure 6 shows the Coulomb attraction energies evaluated from the intercepts of $E_{g(\Gamma-\mathrm{X})} - E_{\mathrm{Coul}} - E_{\mathrm{corr}}$ as a function of crystal size, L_0. The solid line shown in figure 6 shows the result of nonlinear least-squares fitting to equation (6). From that fitting result, $C_{n\ell}$ is estimated as 1.0, which is in rough agreement with the theoretical values of $C_{10} = 3.57$ or $C_{11} = 3.77$ [26].

The results lead us to infer that the ER features located at 1.2–3.1 eV arise from directly assisted transitions at Γ_{v}–X_{c} in Si nanocrystals caused by mixing of wavefunctions that are induced by the break of translational symmetry attributable to the finite size [27, 28].

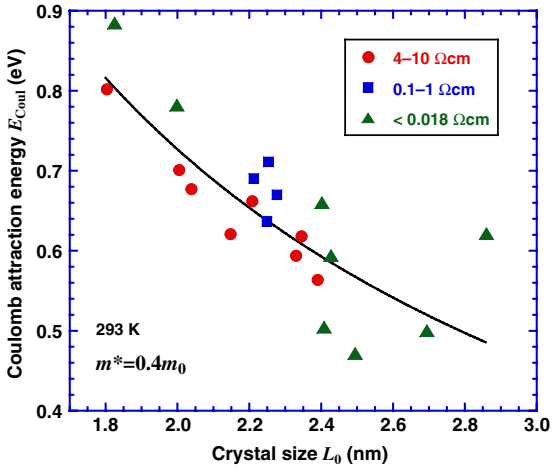

Figure 6. Coulomb attraction energies, E_{Coul}, of Si nanocrystals as a function of crystal size, L_0. Si nanocrystals were fabricated from c-Si substrates with different resistivities (4–10 Ω cm, ●; 0.1–1 Ω cm, ■; <0.018 Ω cm, ▲). The solid line shows the result of nonlinear least-squares fitting to equation (6).

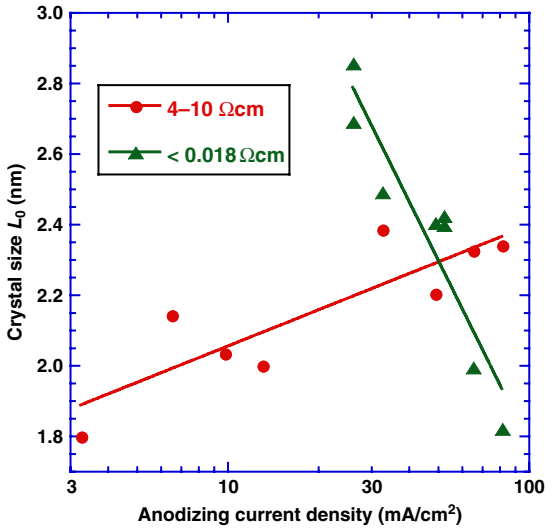

Figure 7. Crystal sizes, L_0, of Si nanocrystals plotted as a function of anodizing current density. The Si nanocrystals were fabricated from c-Si substrates with different resistivities (4–10 Ω cm, ●; 0.1–1 Ω cm, ■; <0.018 Ω cm, ▲). The crystal sizes were estimated from ER measurements.

Furthermore, based on the above analysis, the size of the Si nanocrystals can be estimated from ER spectra without destruction of the sample. Figure 7 shows estimated crystal sizes of Si nanocrystals, L_0, plotted as a function of the anodizing current density, J_{anod}. For Si nanocrystals fabricated from c-Si with a low resistivity of <0.018 Ω cm, L_0 decreases concomitant with increasing J_{anod}, a tendency which shows good agreement with the tendencies of the mean crystal size that are commonly found in porous Si fabricated from c-Si with low resistivity [3].

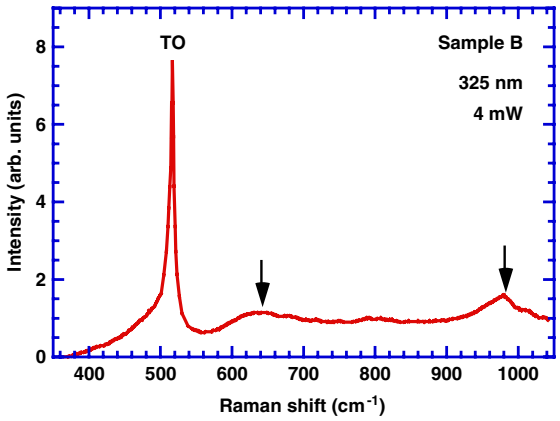

Figure 8. Raman backscattering spectrum of Si nanocrystals (sample B) measured with UV excitation light taken at room temperature. The TO photon peak is readily visible. Arrows indicate the unassigned peaks originating from Si nanocrystals.

3.4. Three-dimensional electronic structure of Si nanocrystals

As described previously, ER features that are readily apparent at around 3.4 eV correspond to optical transitions at $E_1(E_0')$ direct gaps. Figure 8 displays a typical Raman scattering spectrum of the Si nanocrystals excited by the 325 nm line of a He–Cd laser. The Raman spectrum shows a typical asymmetric character at the TO mode with decreased peak frequencies that reflect Si nanocrystals alone [22]; green-laser excited spectra show strong TO-mode signals for c-Si substrates alone. Moreover, the observed peaks at 640 and 980 cm^{-1} are unassigned, as observed for Si nanocrystals [29]. Therefore, the penetration depth for UV light is less than the thickness of the anodized layer, indicating that the three-dimensional electronic structure is retained, even in Si nanocrystals with a mean crystal size of about 1–2 nm.

As described previously, the transition energies of $E_1(E_0')$ direct gaps are almost unchanged against different mean crystal sizes. They are almost equivalent to those of the c-Si substrate. Size effects including the QC effects as well as stress-induced effects do not appear in the bandgap at the $E_1(E_0')$ edge. In addition, the diamond crystal structure is retained in Si nanocrystals as small as 1 nm, as revealed by the TEM images in figure 2. These experimental results enable us to conclude that the electronic structure of Si nanocrystals is slightly modified from that of c-Si. In other words, the three-dimensional electronic structure is retained in Si nanocrystals.

4. Other experimental results

4.1. Effects of impurity doping

Impurity doping usually influences the optical properties of a semiconductor. Employing ER spectroscopy, we have studied optical transitions in Si nanocrystals fabricated from B-doped p-type c-Si substrates with different resistivities, 4–10 Ω cm (p^-), 0.1–1 Ω cm (p) and <0.018 Ω cm (p^+) [16]. The resistivities correspond respectively to boron concentrations of 10^{14}–10^{15} cm^{-3}, 10^{15}–10^{16} cm^{-3} and 10^{18} cm^{-3}. Here, we represent them, respectively, as p^--Si nanocrystals, p-Si nanocrystals and p^+-Si nanocrystals. For ER spectra of p^+-Si nanocrystals, the ER features attributed to confined e–h pairs are also found in the IR–vis region, whereas ER features corresponding to the optical transitions at $E_1(E_0')$ direct gaps are observed at 2.8–3.3 eV. Therefore, the transition energies of $E_1(E_0')$ direct gaps in p^+-Si nanocrystals are shifted down slightly. Figure 9 shows the transition energies of the E_1 direct gaps, which are obtained separately from the energies of E_0' direct gaps by numerical fitting to

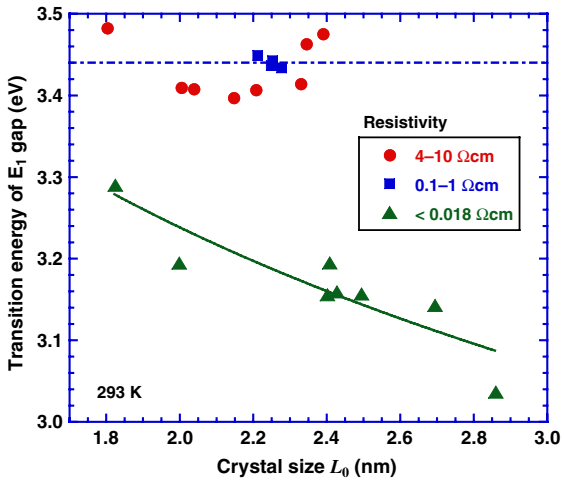

Figure 9. Transition energies at the E_1 direct gaps of Si nanocrystals plotted against the crystal size, L_0. The dotted and dashed line depicts the transition energy of the E_1 gap of c-Si, which is 3.41 eV obtained using ER measurements with an ITO/c-Si diode.

equation (2). Figure 9 shows that, for greater crystal size, the transition energies of E_1 gaps in p^+-Si nanocrystals are smaller, whereas those in p^--nanocrystals and p-Si nanocrystals are equivalent. No pronounced change in the spectral line shape or the peak energy is apparent in the UV-light-excited Raman scattering spectra among the p^--, p- and p^+-Si nanocrystals, indicating that strain-induced and disorder-induced shifts are unlikely to be the major origin for the red shifts in the 3.4 eV ER feature. However, the origin of the red shifts has not been elucidated yet.

We have studied other effects of impurity doping; optical transitions in Si nanocrystals fabricated from p-doped n-type c-Si substrates have been studied using ER measurements [20]. The Si nanocrystals were fabricated by anodization with light soaking, which is usually used for nanostructured porous Si; the anodizing current density was altered to obtain different crystal sizes. Figure 10 depicts the ER spectra of Si nanocrystals fabricated from p-doped n-type c-Si substrates with different anodizing current densities. Two ER features attributed to optical transitions in the confined e–h pair were observed in IR–vis regions. The transition energies reveal that the mean crystal size has a maximum against the increasing anodizing current, as shown in figure 11. Furthermore, ER features arising from $E_1(E_0')$ transitions were weak but detectable at 3.4 eV. Degradation of the $E_1(E_0')$ features arises mainly from temperature broadening; surface roughening is related to line broadening.

4.2. Thermally oxidized nanocrystals

The Si nanocrystals with thermal oxidation usually show strong PL in IR to red regions; the oxidized Si nanocrystals at high temperatures between 800 and 1000 °C often show blue PL [3–5]. Therefore, optical transitions in thermally oxidized Si nanocrystals are also of interest. In the ER spectra of the oxidized Si nanocrystals [18], the E_{10} and E_{11} features appearing in ER spectra between 1.2 and 3.1 eV are found to be insensitive to the degree of oxidation because they come from optical transitions in confined electron–hole (e–h) pairs in Si nanocrystals. Analyses of the transition energies of the IR–vis features reveal that the crystal size, L_0, decreased monotonically with increasing oxidation temperature and/or oxidation time. In contrast, the $E_1(E_0')$ features broaden with higher oxidation temperatures of $>$ about 1000 °C, implying an increase in defects and/or lattice distortion of Si crystals [10].

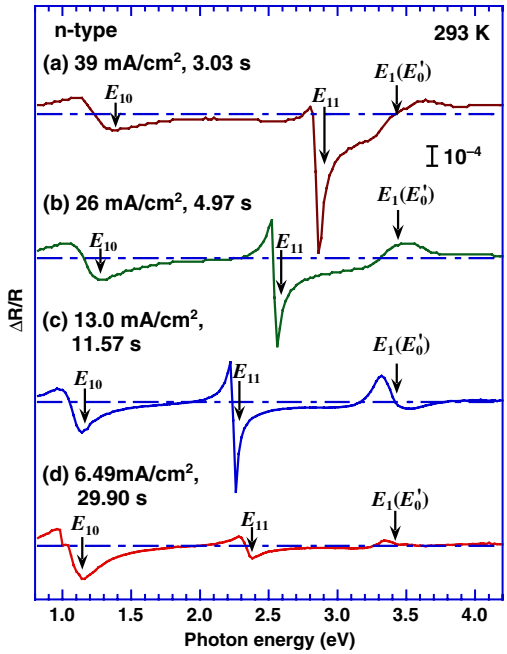

Figure 10. ER spectra of Si nanocrystals fabricated from n-type substrates with different J_{anod} and t_{anod}: (a) $J_{\mathrm{anod}} = 39.0$ mA cm^{-2} and $t_{\mathrm{anod}} = 3.03$ s; (b) $J_{\mathrm{anod}} = 26.0$ mA cm^{-2} and $t_{\mathrm{anod}} = 4.97$ s; (c) $J_{\mathrm{anod}} = 13.0$ mA cm^{-2} and $t_{\mathrm{anod}} = 11.57$ s; (d) $J_{\mathrm{anod}} = 6.49$ mA cm^{-2} and $t_{\mathrm{anod}} = 29.90$ s. The ER spectra are intentionally offset for clarity. Arrows show transition energies estimated from the line shape analyses ($E_{n\ell}$, transitions associated with confined e–h pairs; $E_1(E_0')$, transitions at the direct gaps).

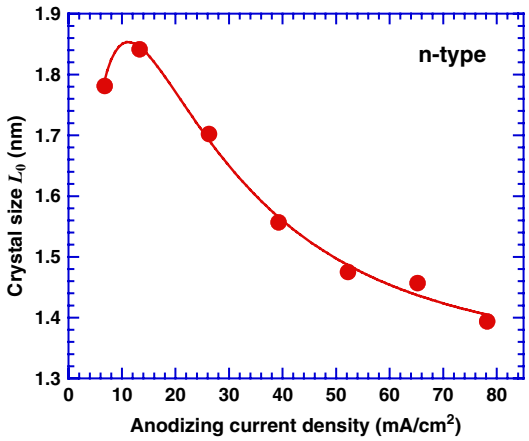

Figure 11. Crystal sizes, L_0, of Si nanocrystals plotted as a function of anodizing current density. The crystal sizes were estimated from the $E_{n\ell}$ transition energies shown in figure 10. The Si nanocrystals were fabricated from n-type substrates. The solid line is presented as a guide for the eye.

4.3. Plasma-deposited thin films

To date, Si thin films deposited by plasma-enhanced chemical vapour deposition have been used widely for thin-film transistors and solar cells [30]. Therefore, Si nanocrystals based on

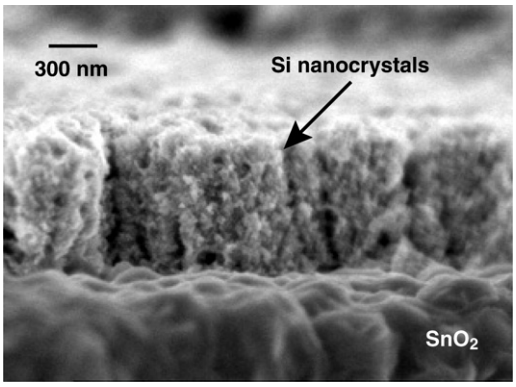

Figure 12. Cross-sectional FESEM image of a Si thin film deposited on a SnO_2 TCO layer. The Si thin film was fabricated by plasma deposition, with subsequent anodization.

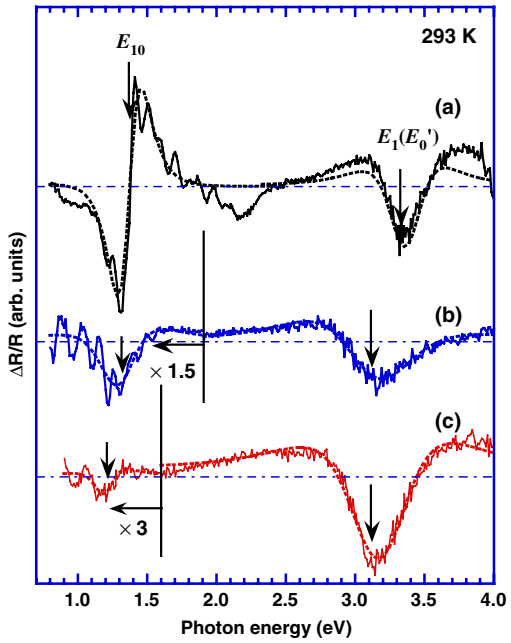

Figure 13. ER spectra of plasma-deposited and anodized Si thin films containing Si nanocrystals with different mean crystal sizes ((a) <2 nm; (b) 2.5 nm; (c) 3.2 nm). ER spectra are measured at 293 K. Dotted lines show nonlinear least-squares fitting results to equation (2). Arrows exhibit transition energies estimated from the line shape analyses ($E_{n\ell}$, transitions associated with confined e–h pairs; $E_1(E_0')$, transitions at the direct gaps).

the plasma-deposited Si thin film can be useful for synthesizing optoelectronic devices on a foreign substrate with a large area. We have fabricated Si nanocrystals from plasma-deposited Si thin films, and characterized them by ER measurements [11–14].

The p-type Si thin films were deposited on SnO_2-coated glass substrates by plasma-enhanced chemical vapour deposition; they were then anodized. The crystal size was changed mainly according to the deposition conditions. The Si thin-film thicknesses were estimated roughly as 0.9–1.4 μm after anodization. Figure 12 shows a cross-sectional FESEM image of the Si thin film after anodization.

Figure 13 depicts ER spectra of the plasma-deposited thin films fabricated with different deposition conditions. From Raman measurements, the mean crystal sizes were calculated respectively as (a) <2 nm, (b) 2.5 nm and (c) 3.2 nm [31, 32]. Although the oscillation fringes attributable to the optical interference are superimposed on the ER spectra, ER features associated with E_{10} and E_{11} transitions in confined e–h pairs appear strongly in the IR–vis regions. With decreasing mean crystal size, the ER features attributed to E_{10} transitions are

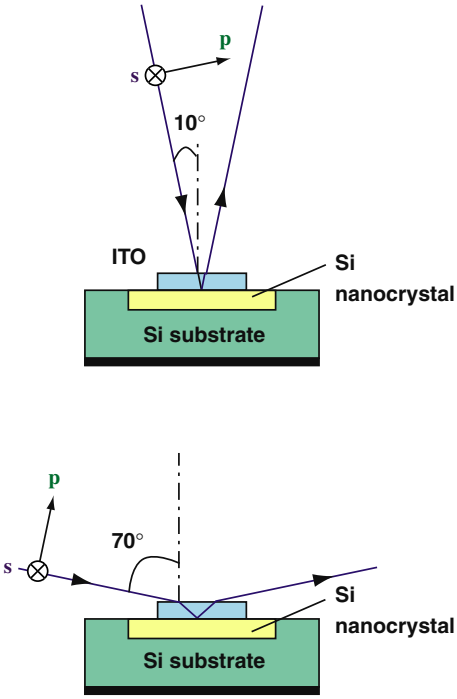

Figure 14. Geometric configurations of ER with polarized incident light, which was applied to the sample at different angles of incidence of 10° (NNI geometry) (top) and 80° (GAI geometry) (bottom).

shifted to blue. On the other hand, the ER features observed between 3.1 and 3.4 eV originate from $E_1(E_0')$ direct gaps. Slight red shifts in the UV features are apparent with increasing mean crystal size, which is associated with heavy boron doping, as described above.

5. Glancing-angle-incident polarized electroreflectance

5.1. Incident-angle dependence

We have introduced an ER measurement technique with glancing angle incident polarized light [19]. Compared to the experimental setup for conventional ER measurements shown in figure 1(a), a polarizer was additionally placed between the monochromator and the sample. Figure 14 illustrates geometric configurations of the incident probe light applied to the sample. The angle of incidence of the probe light was changed from 10° (near-normal incidence (NNI) geometry) to 80° (glancing-angle incidence (GAI) geometry). In NNI geometry, the electric field of s-polarized (p-polarized) light is set as parallel to $[1\bar{1}0]$ ([110]) axis for the (100) c-Si substrate, and to the $[1\bar{1}0]$ ([001]) axis for the (110) c-Si substrate.

Figures 15(a) and (b) show ER spectra of Si nanocrystals in NNI geometry taken at 293 K. The ER spectra were derived, respectively, with s-polarized (a) and p-polarized (b) incident light. Both ER spectra consist of two components in the IR–vis region together with the 3.4 eV component; they are almost identical to the ER spectrum of the sample taken with the conventional setup using NNI geometry and non-polarized incident light.

Starkly contrasting with the spectra described above, the ER spectra of the Si nanocrystals in GAI geometry are shown in figures 15(c) and (d). The ER spectra were also monitored with s-polarized (c) and p-polarized (d) incident light. Compared to the ER spectra in NNI geometry, amplitudes of the ER signals are markedly lower, and the line shapes are broad. As shown in

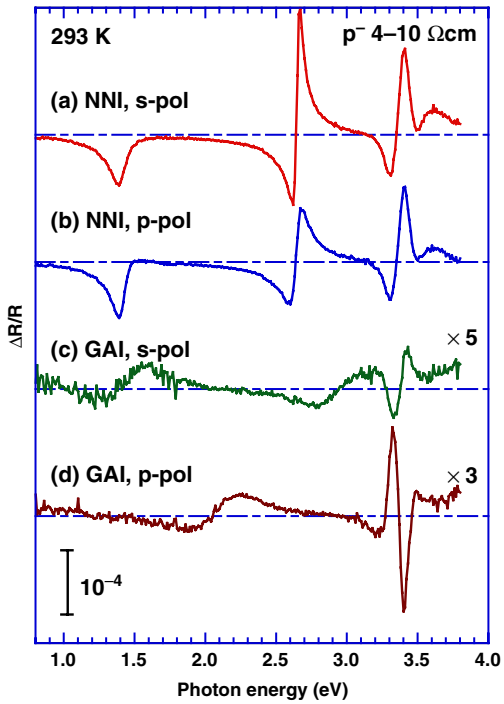

Figure 15. ER spectra of Si nanocrystals taken at 293 K with different configurations (in NNI geometry with s-polarized (a) and p-polarized (b) light, and in GAI geometry with s-polarized (c) and p-polarized (d) light). Curves (c) and (d) are magnified for clarity. Arrows exhibit transition energies estimated from the line shape analyses ($E_{n\ell}$, transitions associated with confined e–h pairs; $E_1(E_0')$, transitions at the direct gaps).

figure 15(c), in the ER spectrum with the s-polarized light, the 1.3 and 2.7 eV features are monitored; their shapes resemble the line shape of the ER spectra in NNI geometry shown in figures 15(a) and (b). On the other hand, in the p-polarized ER spectrum shown in figure 15(d), the 1.3 and 2.7 eV features are not monitored, whereas the 2.1 eV feature is monitored only in the IR–vis region. Therefore, a clear polarization anisotropy occurs in the ER spectrum of Si nanocrystals in GAI geometry; an electric field feature that is parallel to the growth direction of anodized layer (and to the modulation electric field) of the p-polarized light in GAI geometry is responsible for the 2.1 eV feature. Although the actual angle of incidence at the ITO/anodized layer interface is less than the 80° at the air/ITO interface because of refraction, the s-polarized light in GAI geometry, as well as the s-polarized and p-polarized light in NNI geometry, include the electric field component.

5.2. Temperature dependence

Figure 16 shows ER spectra taken in GAI geometry of Si nanocrystals measured after cooling from 293 K to measurement temperatures as low as 4 K. The cooling time was about 1.5 h from 293 to 4 K. After cooling, the sample was maintained at the measurement temperature for 2 h. The ER spectra of the IR–vis region show a drastic transition between 100 and 90 K; the ER spectra measured at $\geqslant$ 100 K contain a single ER feature located between 2.0 and 2.1 eV in the IR–vis region; however, similar to the case of NNI geometry, the ER spectra measured at $\leqslant$90 K consist of the ER feature at 1.5–1.6 eV and the other feature at 2.7–2.8 eV, corresponding,

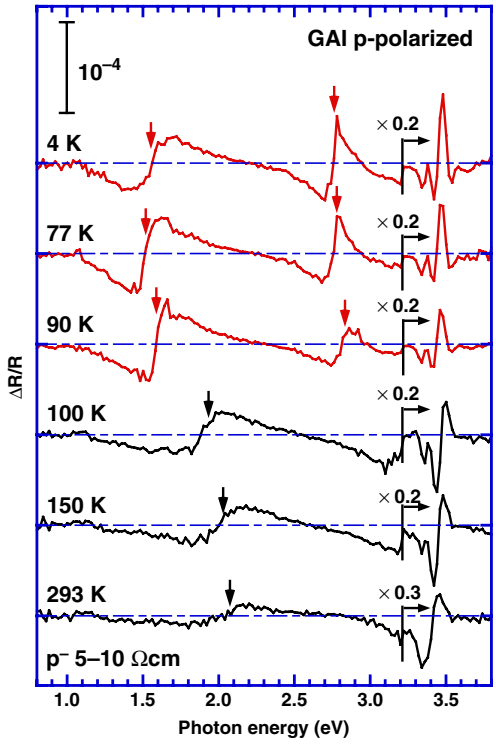

Figure 16. ER spectra of Si nanocrystals in GAI geometry with p-polarized light taken after rapid cooling from 293 K to various temperatures down to 4 K. The 3.4 eV features are reduced in size for clarity. With regard to the ER spectra taken at $\leqslant$90 K, the $E_{n\ell}$ transition energies are estimated from the line shape analyses as exhibited by arrows. The other arrows in the ER spectra taken at $\geqslant$100 K indicate unassigned transitions related to the Si nanocrystals.

respectively, to E_{10} and E_{11} transitions in confined e–h pairs. Such a drastic transition has never been observed for NNI geometry. Moreover, if the sample is cooled gradually, such a drastic transition is not observed. Consequently, rapid thermal quenching and NNI geometry are inferred to be necessary for the drastic transition. On the other hand, regarding the 3.4 eV features, with decreased temperature the transition energies are up-shifted, and the broadening parameters are decreased. As a result, E_1 and E_0' features are observed separately, as shown in figure 16. Nevertheless, the changes in the 3.4 eV feature can be described by the temperature dependence of the 3.4 eV features in bulk c-Si. Therefore, the drastic transition implies that the change in the electronic structure of Si nanocrystals may be located at the anodized layer surface.

6. Conclusions

We used ER spectroscopy to study optical transitions in Si nanocrystals with a crystal size of 1–3 nm. Directly assisted transitions of confined e–h pairs in Si nanocrystals at Γ_v–X_c, which are caused by mixing of wavefunctions that are induced by the break of translational symmetry arising from the finite size, are observed as ER features located between 1.2 and 3.1 eV. Using an EMA model in the strong confinement region, the reduced mass, the kinetic energies and the Coulomb attraction energies of the confined e–h pairs are deduced as a function of crystal size.

Meanwhile, other ER features are found at around 3.4 eV, indicating that the three-dimensional electronic structure remains in Si nanocrystals. ER studies have also been made of samples doped with differently oxidized samples and plasma-deposited samples. Furthermore, to obtain more surface-sensitive measurements, ER measurements with p-polarized incident light in GAI geometry were investigated. The resultant ER spectrum showed an unusual temperature dependence.

Acknowledgments

The authors would like to acknowledge former collaborators Mr Y Kotani, Mr A Shimode, Dr S Abo, Mr Y Nakai, Mr K Moriguchi, Mr A Ogane, Mr T Suzuki and Mr J Ota. This work was supported in part by Grants-in-Aid of the 21st Century COE program (G18) of the Japan Society for the Promotion of Science.

References

[1] Takagi H, Ogawa H, Yamazaki Y, Ishizaki A and Nakagiri T 1990 *Appl. Phys. Lett.* **56** 2379
[2] Canham L T 1990 *Appl. Phys. Lett.* **57** 1046
[3] Lockwood D J 1997 *Light Emission in Silicon From Physics to Devices, Semiconductors and Semimetals* vol 49, ed R K Willardson and E R Weber (New York: Academic)
[4] Vial J-C and Derrien J 1995 *Porous Silicon Science and Technology* (Berlin: Springer)
[5] Feng Z C and Tsu R 1994 *Porous Silicon* (Singapore: World Scientific)
[6] Cardona M 1962 *Modulation Spectroscopy* (New York: Academic)
[7] Hilbrich S, Theiss W, Arens-Fischer R, Glück O and Berger M G 1996 *Thin Solid Films* **276** 231
[8] Pickering C 1994 *Porous Silicon* (Singapore: World Scientific) pp 3–39
[9] Aspnes D E 1973 *Surf. Sci.* **37** 418
[10] Pollak F H 1994 *Optical Properties of Semiconductors* (*Handbook on Semiconductors* vol 2) Completely revised and enlarged edition, ed T S Moss and M Balkanski (Amsterdam: Elsevier)
[11] Toyama T, Kotani Y, Shimode A, Shimizu K and Okamoto H 1998 *Mater. Res. Soc. Symp. Proc.* **507** 243
[12] Toyama T, Kotani Y, Shimode A, Abo S and Okamoto H 1999 *Mater. Res. Soc. Symp. Proc.* **557** 469
[13] Toyama T, Kotani Y, Shimode A and Okamoto H 1999 *Appl. Phys. Lett.* **74** 3323
[14] Toyama T, Kotani Y, Shimode A and Okamoto H 2000 *J. Non-Cryst. Solids* **266–269** 593
[15] Toyama T, Shimode A and Okamoto H 2001 *Mater. Res. Soc. Symp. Proc.* **609** A24.10
[16] Toyama T, Nakai K and Okamoto H 2001 *Mater. Res. Soc. Symp. Proc.* **638** F3.5
[17] Toyama T, Nakai Y, Asano A and Okamoto H 2002 *J. Non-Cryst. Solids* **299–302** 290
[18] Toyama T, Nakai Y, Moriguchi K and Okamoto H 2003 *Phys. Status Solidi* a **197** 482
[19] Toyama T, Nakai Y, Moriguchi K and Okamoto H 2003 *Mater. Res. Soc. Symp. Proc.* **737** 499
[20] Toyama T, Suzuki T, Ogane A, Ota J and Okamoto H 2007 *J. Mater. Sci. Mater. Electron.* at press
[21] Grover J W and Handler P 1974 *Phys. Rev.* B **9** 2600
[22] Irani R R and Callis C F 1963 *Particle Size: Measurement, Interpretation, and Application* (New York: Wiley)
[23] Lautenschlager P, Allen P B and Cardona M 1985 *Phys. Rev.* B **31** 2163
[24] Efros Al L and Efros A L 1982 *Sov. Phys.—Semicond.* **16** 772
[25] Brus L E 1983 *J. Chem. Phys.* **79** 5566
[26] Kayanuma Y 1988 *Phys. Rev.* B **38** 9797
[27] Hybertsen M S 1995 *Porous Silicon Science and Technology* ed J-C Vial and J Derrien (Berlin: Springer) p 67
[28] Brus L 1994 *J. Phys. Chem.* **98** 3575
[29] Fuch H D, Stutzmann M, Brandt M S, Rosenbauer M, Weber J, Breitschwerdt A, Deák A and Cardona M 1993 *Phys. Rev.* B **48** 8172
[30] Tanaka K, Maruyama E, Shimada T and Okamoto H 1999 *Amorphous Silicon* (New York: Wiley)
[31] Richter H, Wang Z P and Ley L 1981 *Solid State Commun.* **39** 625
[32] Campbell I H and Fauchet P M 1986 *Solid State Commun.* **58** 739